

Crossover analysis of Mars Orbiter Laser Altimeter data

Gregory A. Neumann,^{1,2} David D. Rowlands,² Frank G. Lemoine,²
David E. Smith,² and Maria T. Zuber^{1,2}

Abstract. In its first 15 months of continuous operation, the Mars Orbiter Laser Altimeter (MOLA) instrument aboard Mars Global Surveyor ranged to Mars over 330 million times, generating more than 5000 orbital profiles, with a ranging precision of 0.4 m over smooth terrain. The accuracy of the profiles depends on knowledge of the spacecraft position, orientation, and observation time, which are subject to errors. We model these errors via the analysis of over 24 million altimetric crossovers. A quasiperiodic, once per revolution adjustment of the ground tracks as a function of time in three locally orthogonal directions minimizes the altimetric residuals via least-squares. Using a sparse matrix technique, computational effort scales linearly with the number of crossovers and only marginally with the number of parameters. Orbital errors mainly result from poor modeling of spacecraft thrusting events in the absence of tracking. Seasonal effects, likely due to changing thermal environment, as well as residual miscalibrations, are evident in the pointing solutions. Incorporating multiple parameters per revolution significantly improves crossover residuals, and resolves pointing aberrations during orbital transitions from night to day. Altimetry from the adjusted tracks generates a topographic model whose accuracy is typically better than 1 m vertically with respect to the center of mass of Mars. The centroid position of each MOLA shot is typically accurate to ~ 100 m horizontally. Terrain models from accurately located lidar data can be gradient-shaded to illuminate geological structures with 1 in 1000 slopes that are invisible to cameras. Temporal changes in elevation (e.g., frost deposition/ablation) at decimeter levels may also be assessed using crossovers, but results must be interpreted with caution due to uncertainties in range walk correction.

1. Introduction

The Mars Orbiter Laser Altimeter (MOLA) [Zuber *et al.*, 1992; Smith *et al.*, this issue], an instrument on the Mars Global Surveyor (MGS) spacecraft, is currently measuring the global shape and surface properties of Mars. MOLA operated intermittently during 1997-1998, continuously from March 1999 to shutoff in June, 2000 for solar conjunction, and was restarted in August. This study addresses data acquired in the mapping configuration, from February 28, 1999

to June 1, 2000.

The MOLA laser fires ten pulses of $1.064 \mu\text{m}$ wavelength light per second while MGS orbits Mars in a near-polar, circular orbit. The receiver measures the two-way time-of-flight, to provide a range. The MGS orbital period of ~ 7060 s provides more than 12 altimetric tracks per day. Typical MOLA ranges have a precision and accuracy of 37.5 cm after correction for pulse spreading and system response [Abshire *et al.*, 2000]. More than 95% of returns result from ground echoes, while clouds and noise make up the rest. A ground track consists of ~ 168 -m-diameter footprints at a nominal 400 km spacecraft altitude, spaced ~ 300 m apart. Individual profiles, collected over many months, are assembled into global terrain models [Smith *et al.*, this issue]. High

¹Department of Earth, Atmospheric and Planetary Sciences, Massachusetts Institute of Technology, Cambridge, Massachusetts, USA.

²Laboratory for Terrestrial Physics, NASA Goddard Space Flight Center, Greenbelt, Maryland, USA.

precision notwithstanding, MOLA profiles exhibit systematic mismatches due to errors in spacecraft timing, position, and attitude that could be misinterpreted if not appropriately corrected. In this analysis we use altimetric crossovers to improve significantly the locations of laser shots on the Martian surface, modeling the combined effects of orbit and pointing error. We identify the radial, along-track, and across-track errors on each profile. Correcting these errors leads to a globally consistent, high-accuracy, topographic field. We first present some details of the data analysis not covered elsewhere, and describe random and systematic sources of error particular to the MOLA instrument. We then modify the approach of *Nishimura and Forsyth [1988]* to model the combined effects of orbit and pointing error in a very large dataset. A synthetic example demonstrates the resolution of these errors in three components.

1.1. Crossovers

Altimetric crossovers are the difference between the radial distance (or height) of two distinct ground tracks at a common location - generally an ascending and descending track (Figure 1). Owing to the rotation of Mars, many such crossovers occur at all latitudes, intersecting at angles of 15° at the equator. For closely spaced footprints the difference in altitudes at the intersection may be found by linear interpolation. This difference constrains the vertical position error along the ground tracks.

Crossovers have been used as an observation of the spacecraft radial position in the orbit determination process [e.g., *Shum et al., 1990*]. Experience with the use of crossovers in satellite geodesy includes Earth-orbiting radar altimeter satellites, such as TOPEX [*Marshall et al., 1995*]. MOLA crossovers were first used during the initial MGS orbit insertion mission phase as an observation type to improve orbit and attitude determination in a joint solution with Doppler tracking [*Rowlands et al., 1999*]. More recently, altimetric crossover data from selected mapping observations have been used to improve the Martian gravity field [*Lemoine et al., this issue*]. Conversely, each improvement in gravity field has resulted in improvements in the quality of orbits, and thereby an ongoing reduction in crossover error.

Crossover analysis provides an important measure of data quality, since over a solid surface, neglecting tides and seasonal surficial changes, the altitude of the ground spot is constant. Conversely, crossovers may be used to assess temporal changes in topography (D. E. Smith et al., manuscript in preparation, 2001) or rotational dynamics [*Zuber et al., 2000*].

Over rough terrain, pointing and horizontal position errors also contribute to crossover discrepancies. Laser altimetry, where a narrow beam is directed to a spot on

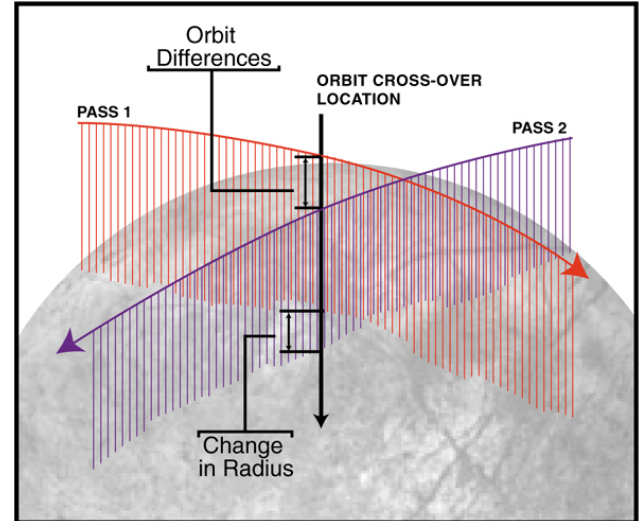


Figure 1. Schematic illustration of altimeter crossover approach. The objective is to measure, at points where two orbits cross, the range from the spacecraft to surface from altimetry and the radius of the spacecraft from the planetary center of mass from Doppler tracking. By minimizing the misfit of many crossings in a least squares sense both the orbits and the topographic field can be improved.

the ground, differs markedly from radar altimetry (e.g., GEOSAT, Venus-Magellan). Radar altimetry has a wider effective footprint and is essentially nadir-pointing. Laser altimetry is particularly sensitive to pointing errors and horizontal orbit errors over sloping terrain, given that laser footprints are generally small relative to the spacing of the observations, and can resolve significant ($>30^\circ$) slopes.

Controls on pointing may be obtained through roll-and-pitch maneuvers on missions such as the Shuttle Laser Altimeter [*Garvin et al., 1998*] and future missions (e.g., the Geoscience Laser Altimeter System and Vegetation Canopy Lidar) by using the ocean surface as a reference [*Luthcke et al., 2000*]. Such methods are less appropriate for Mars, where terrain is unknown and extent of flat surfaces is limited. This study, like that of *Rowlands et al. [1999]*, exploits naturally sloping terrain and shows that, given sufficient data, a global crossover analysis in nadir operation can simultaneously correct for pointing and orbital error, even as these errors vary with time.

1.2. Elliptical Orbit Results

During the orbit insertion phase of the MGS mission (the suspension of aerobraking in 1997 known as Hiatus, and the Science Phasing Orbit subphases SPO-1 and SPO-2) the

MGS orbit was highly eccentric, with an altitude at periapsis of ~ 170 km, reaching $>21,000$ km at apoapsis. MOLA ranged to the Northern Hemisphere for ~ 25 min on each orbit. Off-nadir operation was performed during a few of these passes in order to resolve topography up to the poles, and for targeting purposes. These operational modes were not considered in detail in the original science plan [Albee *et al.*, 1992]. The orbital eccentricity and rapid slews off-nadir revealed significant timing and attitude biases aboard MGS at this time.

The profiles collected during Hiatus [Smith *et al.*, 1998] did not intersect. As the MGS periapsis evolved during aerobraking, many crossovers occurred. At the outset of SPO-1, there was a sloping trend to the residuals versus time. On approach to the planet, altimetry appeared lower than expected, while the opposite was true as the spacecraft receded. In an eccentric orbit an offset in the timing of the laser pulses produces a systematic slope in the profiles, with an origin at the time of periapse. The slope was eliminated by adding ~ 117 ms (30/256 s) to the laser firing time. The precise cause of this apparently constant shift remains unknown, but in all further discussion, laser fire time is taken to be 117 ms after the time recorded in the MOLA Precision Experiment Data Record (PEDR).

From a series of off-nadir observations, Rowlands *et al.* [1999] estimated significant roll and pitch offsets in the instrument boresight alignment relative to the spacecraft. An apparent shift of half a milliradian from preflight values caused topography to appear lower when ranging to one side of nadir, and higher to the other. Furthermore, they found a systematic delay in the attitude data. Normally, the spacecraft rotates at ~ 0.9 milliradian per second in inertial coordinates to maintain nadir orientation. In this mode, a timing delay is virtually indistinguishable from an offset in pitch angle. During rapid slews the attitude timing bias is much more apparent and can be characterized uniquely. The delay was traced to the spacecraft attitude control system (ACS). The ACS filters the output of star trackers, horizon sensors, and gyro sensors to maintain stability, and relays the filtered output at reduced rate to the ground. A side-effect of the filter is a causal delay, with a rate-dependent phase response, resulting in the time stamp being applied to measurements of the orientation matrix taken somewhat earlier. The inferred discrepancy is, in principle, correctable, but in the presence of noise a full correction is unstable. As a workaround, these delays were corrected in the pre-mapping period by adding 1.15 s to the time for which the pointing matrix is desired, [e.g., Rowlands *et al.*, 1999]. During the mapping mission phase, changes were made to the filter parameters that should have increased the delay to 2.3 s (W.J. Glance, written communication, 1999), and the archival C-kernels

were adjusted by this amount. However, the delay appears to remain at the pre-mapping value both in normal mapping mode and during higher slew-rate maneuvers, and the nominal timing bias of 1.15 s was applied.

2. Data

The volume of planetary range data acquired during the first three days of mapping exceeded that from all of the previous 17 months of aerobraking. In this study, only ranges with angles less than 0.02 radians from nadir with respect to the MGS radius vector are employed. Some ranges were targeted up to 49° off-nadir to fill in the poles, but their treatment is beyond the scope of this work.

2.1. Orbital, Attitude and Planetary Orientation Data

Precision orbits are crucial to producing highly accurate topographic profiles. Orbits are constructed from range and Doppler tracking from NASA's Deep Space Network (DSN). Apart from certain campaigns, tracking is discontinuous, generally consisting of one DSN pass per day, and orbits are determined dynamically. MOLA orbits are calculated using the Goddard Space Flight Center GEODYN orbit determination software [Ullman, 1997; Pavlis *et al.*, March 26, 1999]. The processing uses refined gravitational models of Mars [Lemoine *et al.*, this issue; Smith *et al.*, 1999a], detailed models of the effects of nonconservative forces such as solar radiation pressure, Mars solar reflected radiation and thermal emission, and atmospheric drag [Lemoine, 1992; Lemoine *et al.*, 1999], as well as other effects such as the third body perturbations due to the Sun, the planets, and the moons of Mars. Accelerations due to periodic thrusting events aboard the spacecraft are estimated.

GEODYN generates a spacecraft ephemeris over ~ 7 -day arcs, offset by 5 days to allow overlapping comparisons. The orbits are archived as evenly-spaced, discrete states every 20 s, and accessed by the NAIF SPICE software [Acton, 1996] using Lagrange interpolation. Orbits were refined continuously throughout the first year of MGS mapping as knowledge of the gravity field improved, and more refined nonconservative force models were implemented [Lemoine *et al.*, this issue]. Radial errors in independent orbit solutions at overlaps are typically less than 1 m but exceed 10 m where tracking is sparse. Along-track and across-track overlaps are typically less than 10 m but may exceed 100 m. The variable quality of the orbit determination process mandates consideration of altimetry either in the orbit analysis directly, or afterwards as in this study.

2.2. Nonorbital Error Sources

Timing and attitude reconstruction are supplied by the spacecraft ground system at Lockheed-Martin Astronautics in Denver, via the MGS Project. Pointing matrices from the filtered attitude data transform the instrument boresight direction to the J2000 inertial frame. MOLA ranges are projected from the spacecraft states at the laser transmit and receive times along the instrument boresight to locate the laser bounce point in the Mars center of mass inertial frame. The bounce point is then transformed to body-fixed coordinates using the IAU1991 [Davies *et al.*, 1992] planetary orientation model.

The altimetric error budget depends strongly on observation geometry, timing, and range precision, as well as orbital accuracy. The most favorable lidar mode is nadir-pointing, in a near-circular orbit. The MGS mission was planned with this in mind, and its 92.87° inclination permits more than 99% of the planet to be mapped in this mode. MGS maintains nadir orientation as it circles the planet, minimizing the impact of pointing errors on measurements of the planetary radius. Given the several kilometer wide spacing of MGS ground tracks, the baseline pointing knowledge of 3 milliradians [Zuber *et al.*, 1992], or 1.2 km on the ground from an altitude of 400 km, is adequate for global characterization of shape, but for detailed studies, e.g., of landing sites, better knowledge is desired.

Timing is of first-order importance for altimetry from a satellite whose motion over the ground exceeds 3 km s^{-1} , and whose inertial angular velocity is $\sim 1 \text{ mrad s}^{-1}$. Laser ranges are the time of flight of a pulse of light, measured by an internal time source, multiplied by the speed of light. Refinements to the timing reconstruction process are presented in Appendix A, providing absolute range calibration and minimizing timing errors.

Ranging is affected by the dispersion of laser pulses by the ground, occasional clouds, and by the system response of the detector. MOLA processing applies corrections for distortion of the laser pulse according to the receiver model of Abshire *et al.* [2000]. Analysis of the first year's data provides some insight into the accuracy of such corrections along profiles.

2.3. Range Calibration and Saturation

In leading edge range detection, the tendency for stronger and/or wider optical pulses to trigger earlier than weak ones, and thereby bias altimetry upward, is known as range walk. The precision of the time-of-flight measurement is $\sim 2.5 \text{ ns}$, corresponding to an elevation of 37.5 cm. The time t_{le} between the leading edge and the center of the pulse is an order of magnitude greater. A correction of several meters for

range walk and system delays, multiplied by the cosine of the emission angle from the ground, is applied to the planetary radius for each shot. These corrections are a potential source of systematic errors in the altitude of the bounce point. The effect of these corrections on the horizontal position is insignificant at the scale of a MOLA footprint.

The detailed calibration of the MOLA range and pulse parameters are presented in Abshire *et al.* [2000]. Their receiver model compensates for range walk by adding half the measured pulse width to the time of flight, assuming a symmetric waveform. We briefly discuss this model, and possible errors therein affecting crossovers, via the statistics of large numbers of data from mapping.

The outgoing pulse width is 8-20 ns full width at half maximum, depending on laser output [Afzal, 1994]. Footprint scale slope and surface roughness disperse the returning photons in time. The output of the MOLA detector passes through four parallel filter channels to reduce its noise bandwidth, further spreading the pulse. MOLA measures the two-way time of flight to the leading edge of a pulse on the first filter channel to exceed its threshold voltage y . After each trigger, pulse width W_y and energy A_y are measured to the crossing of the threshold voltage by the trailing edge of the pulse, providing some information on the waveform. The measurements of width and energy, using separate ranges on each channel, are fairly coarse, with a precision of 6 and 8 bits, respectively, and report maximum values of 63 and 255 when their dynamic range is exceeded. The detector amplifier runs at a fixed gain, so it is possible for very strong pulses to exceed its linear range of response. It is believed that this "clipping" occurs only after the energy measurement has reached its maximum value of 255. This condition, called saturation, frequently occurs over very flat ground due to the fact that all of the energy is returned in a very narrow period of time. Since it is impossible to know whether the pulse has been distorted when the energy count is 255, we refer to all such pulses as saturated.

Channel 1, with the highest bandwidth filter (20 ns), makes up 88% of ground triggers in mapping, and channel 2 (60 ns) makes up $\sim 12\%$, with a few triggers over very steep slopes detected on the remaining channels. Owing to the unexpectedly flat topography of Mars, channels 1 and 2 were, on average, saturated in energy 70% of the time and 36%, respectively. As the laser output declined, and the atmospheric opacity increased, channel 1 did not trigger as often, and as many as 25% of returns came from channels 2 and higher. The number of saturated pulses varied with laser output and atmospheric conditions, so that by June 2000 only 60% were saturated on channel 1.

Over flat ground, the range walk correction for channel 1 is typically of the order of 3 m of altitude, and for the weak-

est pulses returned, is only 1 m. Under ideal conditions, the uncertainty of this correction is on the order of 30 cm [Abshire *et al.*, 2000]. This uncertainty applies only to ranges for which neither the energy nor pulse width are saturated. For the bulk of the mapping data, $\sim 2/3$ of all pulses were saturated. Under such conditions the pulse waveform becomes skewed due to nonlinearities in the electronics, and the pulse width measurement may increase erratically toward its maximum value, resulting in an altimetric correction of up to 7.5 m. This erratic behavior is especially evident over the smooth polar caps.

Two measures were adopted to mitigate this problem. First, on July 1, 1999, the minimum threshold for channel 1 on the instrument was raised to 0.56 V, near its maximum setting, from its floating setting of 0.1 to 0.25 V, making the energy and pulse width measurements somewhat smaller and reducing the number of false triggers. This made the pulse width measurements less likely to saturate but did not significantly affect the energy saturation problem. Second, rather than always using the pulse width on channel 1 from saturated-energy returns as a correction in processing, the pulse spread G (1σ) was estimated from the along-track slope and receiver characteristics via the Gardner [1992] equation, and applied as an upper limit to the correction. The pulse spreading is generally greater than given by Gardner due to intrinsic surface roughness. Furthermore, the triggers usually occur well before the steepest portion of the rising pulse waveform, so that $W_y/2$ is greater than the 1σ pulse width. Because of these considerations, a leading-edge timing correction of 20 ns [Abshire *et al.*, 2000, Table 5] was applied as an absolute lower limit over smooth ground. The range walk $t_{1e} = \min(G', W_y/2)$, where estimated pulse half-width at threshold is $G' = \max(G, 20)$. The leading-edge correction is a minimum estimate, shortening ranges and biasing topography upward. When link margin is reduced, as when clouds or opaque atmosphere intervenes, topography appears lower.

We can quantify the effect of miscalibration in saturation by comparing topography from adjacent shots resulting from different channels. We first compare only unsaturated shots from channel 1 with unsaturated shots from channel 2, with presumably symmetric pulse waveforms, and then saturated shots from channel 1 with unsaturated channel 2. On level ground, the difference should approach 0. The distribution of differences is very long-tailed due to topography, so we characterize it with several measures of central tendency.

Table 1 gives the following topographic differences (channel 1 - channel 2, in meters). Here the mode is taken to be the least median of squares (LMS), the midpoint of the smallest interval to contain at least half the observations. Clearly, the tendency is for altitudes from saturated ranges to appear

Table 1. Topographic Comparison of Channel 1 Shots Adjacent to Channel 2^a

Type	Mean	Median	Mode	No. of Pairs
Channel 1 saturated	0.90	0.34	-0.30	621,330
Channel 1 unsaturated	-0.19	-0.30	-0.53	10,855,192
difference	1.09	0.64	0.23	...

^aComparisons in meters.

higher by 0.23 to 1.1 m. We interpret this as mainly due to the use of a minimum estimate of range walk in saturation. This may introduce significant crossover error as atmospheric and/or ground characteristics vary with time.

The second row of Table 1, comparing unsaturated data, suggests a bias between channels 1 and 2, a further potential source of error. The zero-range bias calibration [Abshire *et al.*, 2000] has subsequently been fine-tuned to remove this bias.

2.4. Clouds and False Returns

Orbital accuracy must be analyzed with true ground returns. MOLA generates about 1-2% false triggers, due to the adaptive threshold algorithm used to maximize the probability of detection [McGarry *et al.*, 1991]. Additionally, many clouds on Mars are sufficiently reflective to trigger the detector before the ground is reached. For example, in the month of October 1999, $\sim 33,000$ cloud returns were detected, $\sim 0.15\%$ of all returns. Noise and clouds triggers occur on all channels, and may appear anywhere from a few meters above the ground to over 15 km. The highly variable topography of Mars, with measured slopes exceeding 45° , makes it difficult to distinguish clouds at low elevations from ground simply from a general knowledge of the terrain.

The detection and removal of clouds is performed in two stages. In the initial, automated processing, a recursive, terrain-following algorithm [cf. Smith *et al.*, 1997] edits the majority of clouds and noise. This algorithm tracks the median and inter-quantile scale statistics of slopes over ~ 2 s windows of time. Asymmetric criteria track down the walls of craters and rifts, while rejecting almost all clouds. Figure 2 shows a ground profile and the limits of acceptance of the filter forward in time. The limits increase where the dispersion of slope values is greater and over gaps in ground shots. The upper range barely tracks the ascending wall of a large crater but excludes a cloud just above its rim. Filtering in reverse recovers ground points that are missed. Automatic

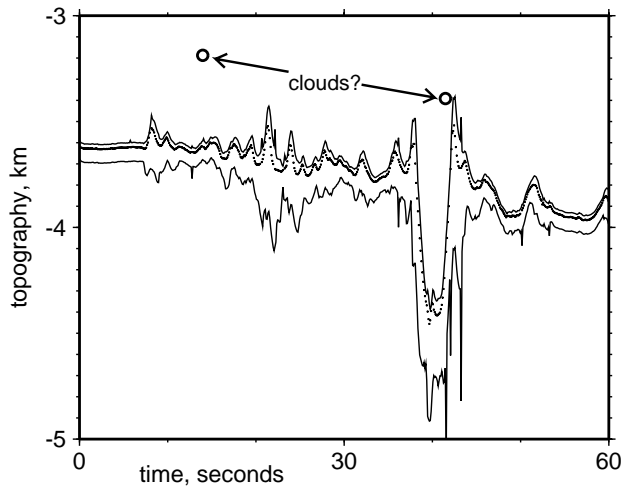


Figure 2. Typical profile showing ground (crosses) and noise (circles) returns. Adaptive algorithm increases its limits (upper and lower curves) based on the local roughness of terrain. Several noise returns lie outside the plotting window.

filters may not follow terrain well through gaps in telemetry and long intervals of clouds. Manual editing corrects most mistakes, but in the more than six million data points generated each week, a handful of errors and ambiguities may remain.

3. Crossover Error Minimization

Traditionally the crossover problem is posed as the elimination of bias and/or drift for gravity or altimetry on a given oceanic or orbit track [e.g., *Prince and Forsyth, 1984; Menke, 1989*]. The bias parameters may be found by solving a set of normal equations by least-squares, resulting in a dataset with reduced errors. *Wessel [1989]* solved for a linear drift function for each of many tracks, using an iterative solution algorithm that does not require reduction of large matrices. This approach was used during the orbit insertion phase of MGS but does not correct horizontal position error nor is it applicable to continuous mapping.

In marine bathymetry the "altitude" of the sensor is well known, but the geographic position of the ship may be uncertain. Prior to the full deployment of Global Positioning Satellites, considerable effort by hand was required to match up swaths on successive cruises. A formalism for this was introduced by *Nishimura and Forsyth [1988]*. A relative position estimate with formal errors was obtained at each intersection of swaths by minimizing bathymetric residuals. The relative position solutions were combined with occasional position estimates from the Transit satellite system and crossings with later, well-navigated cruises to derive a

smooth navigational correction function parameterized by time, from which accurate charts could be made. Such a function is crucial for gravimetry, since Eötvös corrections depend on speed and heading. Two parameters were introduced for each crossover, and one for each navigational fix, with smoothness constrained by a Gaussian covariance. As the number of parameters grows, so do both dimensions of the normal matrix. The matrix bandwidth expands with the distance in time between crossing tracks, leading to a polynomial growth of computational effort with the number of crossovers. This problem is addressed in the next section.

Neglecting off-nadir maneuvers, each orbit track intersects every other approximately twice, for $n(n-1)$ crossings, where n is the number of orbits. Thus the number of crossovers grows quadratically with time, and computing them consumes considerable resources. The XOVER system of [*Wessel, 1989*] locates ground-track crossings of distinct orbital tracks, chosen so that the maximum gap between adjacent ground points on either track is less than 0.2 s (two shot spacings), or ~ 600 m. Linear interpolation of altitude h over this distance may introduce random errors in rough terrain. Flat regions allow close comparisons at many crossovers, but the distribution of random errors has very long tails. Crossovers with excessive (>0.1) point-to-point slopes and wildly discrepant crossover residuals are excluded. Figure 3 shows the typical distribution of crossover locations. Crossovers occur at all latitudes, but density is greatest over smooth terrain and where tracks converge at the poles.

At each crossover we obtain the altimetric residual

$$d(t, t') = h(t) - h(t') \quad (1)$$

at a time-ordered pair of crossover times t, t' , as well as the latitude, longitude, and a pair of headings and slopes. Each slope samples the topographic gradient at the estimated crossover point along its heading, over a 300-m baseline (assuming a constant ground velocity of 3 km s^{-1}). Two slopes suffice to determine the terrain gradient at a point. In many regions, especially near the poles, tracks are nearly collinear and the cross-track slope is poorly resolved, but as the number of orbits increases, the number of independent crossing data grows quadratically and the effective resolution increases in a linear fashion.

3.1. Method of Least Squares Adjustment

Figure 4 shows crossover residuals as a function of time for a typical day (12.24 orbits on September 8, 1999). The density of crossovers is greatest at the poles. The crossover errors are dominated by a quasiperiodic signal, occurring once per revolution, but changing abruptly at several points

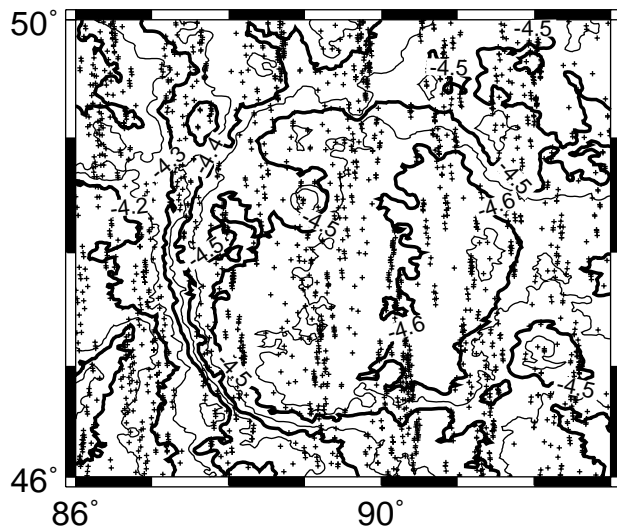


Figure 3. Distribution of crossover locations (crosses) over an unnamed, 200-km-diameter crater in Utopia Planitia. Minor contour interval is 50 m. Crater relief is less than 300 m from rim to floor, with slopes too subtle to be detected by imaging. Identification of such features depends on accurate topography constrained by crossovers.

in time. Furthermore, the signal baseline shifts by several meters. Symbols denote the times of angular momentum desaturation events (AMDs). Thrusting events, which occur autonomously several times per day, change the pattern of crossover error. Where constrained by tracking, the orbit determination process solves for these accelerations, but tracking is often interrupted for periods of up to 18 hours.

The software of *Wessel* [1989] uses a linear function to correct for systematic offset and drift. Such corrections were applied to the earliest MOLA data released during orbit insertion, requiring two parameters per track. A linear function was unsuitable, however, for the continuous orbital coverage in mapping. A smooth function of time that corrects the errors on crossing tracks at widely separated times is required.

A least-squares formalism was introduced by *Nishimura and Forsyth* [1988], using linear combinations of Gaussian basis functions to assure smoothness. This formalism requires two constraint equations for each dimension at each crossover. Each equation must span crossovers over at least one orbital period. With millions of crossovers, the resulting matrix is very large. Motivated by the success of the approach of *Nishimura and Forsyth* for smaller datasets, we adopt a set of regularly spaced, compact functions as a basis for adjustments in each of three dimensions (3-D), limiting the number of independent model parameters to some mul-

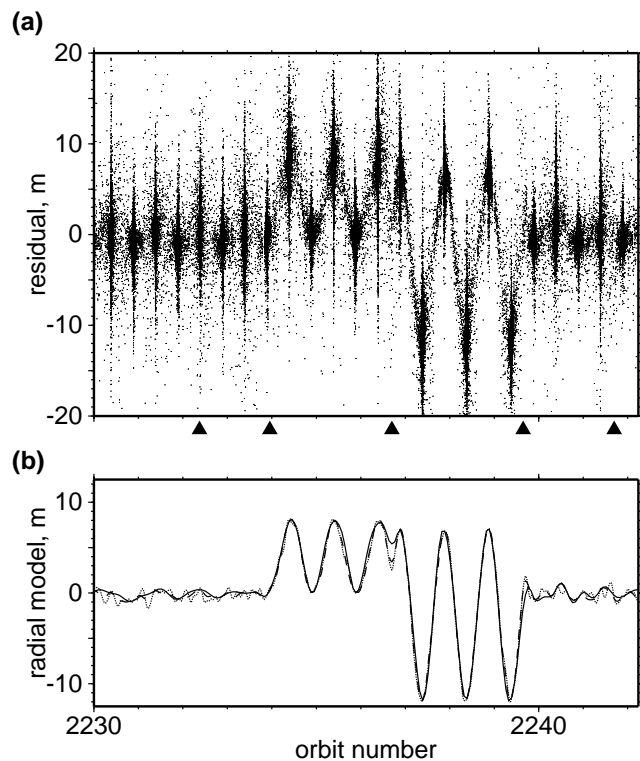


Figure 4. (a) Crossovers versus time over one Earth day. For clarity, the residuals are shown with respect to ground tracks that have already been adjusted. (b) Curves show models using four (solid), eight (dashed), or sixteen (dotted) parameters per revolution to fit altimetric residuals. Times of known propulsive events are shown by symbols.

multiple of the number of orbits. These parameters are further constrained to covary with zero mean [e.g., *Tarantola and Valette*, 1982] so that in the absence of data, the adjustment function tends smoothly to zero.

3.2. Radial Adjustment

A simplified 1-D method, modeling only radial errors, illustrates our 3-D approach. Ideally we would employ enough parameters to characterize any smooth function, especially harmonic functions of the orbital period, but not so many as to be unstable or computationally intractible. The radial adjustment function $g(t)$ is parametrized as the sum of overlapping basis functions scaled by coefficients p . A basis function with compact support is desirable to minimize the bandwidth of the solution algorithm. A "raised cosine" $1 + \cos(\theta)$ in the domain $-\pi$ to π suffices to generate any sinusoidal harmonic by summing terms of alternating sign, shifted by $\pi/2$. Four alternating terms per revolution generate piecewise a sinusoid of arbitrary phase, while coeffi-

coefficients of like sign generate a superimposed low-frequency background. For simplicity in evaluation we approximate one cycle by a polynomial in the domain $[-2, 2]$:

$$f(x) = 1 - \frac{x^2}{2} + \frac{x^4}{16} \quad (2)$$

and zero elsewhere, using

$$x = 4(t - t_0)/r \quad (3)$$

as a normalized time coordinate, where r is the duration of one cycle (a revolution or fraction thereof), and t_0 is a convenient origin time.

The value of the adjustment is

$$g(t) = \sum_{j=m-1}^{m+2} p_j f(x - j), \quad (4)$$

where m is the greatest integer less than or equal to x . The function g is linear with respect to p and we may define its operation vectorially as

$$g(t) = \mathbf{G}_i \mathbf{p}, \quad (5)$$

where the i th crossover datum occurs at time t , and

$$\mathbf{G}_{ij} = \frac{\partial \mathbf{G}_i}{\partial p_j} = f(x - j). \quad (6)$$

The kernels are non-zero for normalized time only within the domain $x \in [j - 2, j + 2]$.

Since a crossover residual $d(t, t')$ results from track positions at two widely separated times, we assign to each crossover two artificial data values in the residual vector $\Delta \mathbf{d}$, of opposite sign, at t and t' :

$$\Delta d(t) = +d(t, t') - g(t) + g(t') \quad (7a)$$

$$\Delta d(t') = -d(t, t') + g(t) - g(t'). \quad (7b)$$

We assume that the residual at time t is insensitive to the adjustment at t' , in other words, that the adjustment $g(t')$ is already constrained. Our strategy is to trade rigor for reduced bandwidth, and iterate to a solution. This device leads to a very sparse system of equations as described below.

Ignoring the correlation of data residuals $\Delta d(t)$ and $\Delta d(t')$, we set the data covariance to the identity. On the basis of the 0.85-m quality of orbit overlaps [Lemoine *et al.*, this issue], we set a priori standard deviations for the radial orbit error parameters p_j at 1 m, with an expectation of zero. These choices are not critical since, as shown below, the problem is heavily overconstrained. Since the orbit error may be parametrized with an arbitrarily dense set of basis

functions, and we desire solutions to be smooth, i.e., have a minimum overall mean-squared slope, we minimize the difference between the coefficients of adjacent basis functions, with a standard deviation of 1 m. These two conditions may be expressed as an inverse covariance, or constraint matrix \mathbf{C}_{pp}^{-1} , whose elements are the model standard deviation reciprocal squared, plus terms that express a centered difference of adjacent parameters. These terms are built up by summing submatrices:

$$\begin{array}{cc} 1 & -1 \\ -1 & 1 \end{array}$$

offset by one index, so that each interior row contains

$$(\dots \quad -1 \quad 2 + \sigma_p^{-2} \quad -1 \quad \dots).$$

The solution at the $(k + 1)$ th iteration is obtained from [Tarantola and Valette, 1982]:

$$\mathbf{p}_{k+1} = \mathbf{p}_k - (\mathbf{G}^T \mathbf{G} + \mathbf{C}_{pp}^{-1})^{-1} (\mathbf{G}^T \Delta \mathbf{d} + \mathbf{C}_{pp}^{-1} \mathbf{p}_k), \quad (8)$$

where the superscript T denotes the matrix transpose. Because the half-bandwidth of these normal equations is just four terms for each parameter, or twelve terms for a 3-D adjustment, the matrix product can be stored in an upper-triangular banded form to conserve memory. A Cholesky decomposition [Press *et al.*, 1992] quickly evaluates the inverse. The data residual $\Delta \mathbf{d}$ is calculated from (7) using the parameter vector \mathbf{p}_k at the k th iteration. Equation (8) then jointly minimizes the solution size $\mathbf{p}^T \mathbf{C}_{pp}^{-1} \mathbf{p}$, and the sum-squared error $\Delta \mathbf{d}^T \Delta \mathbf{d}$.

Initially, crossover residuals are accepted up to 330 m. After each iteration, the residuals are recalculated using (7). The criterion for excessive crossover error is successively reduced, until crossovers with no more than 10 m of error are accepted. In other words, each track is shifted toward its true position, and (8) is solved again. To assure stable convergence, the solution perturbation is damped by a factor less than unity, since the artificial data residuals are overstated and can lead to oscillations in some pathological cases. As iterations converge, the number of acceptable crossovers stabilizes or even increases, while the data residual decreases. A dozen iterations reduce the crossover error close to its final value, but further iterations increase slightly the number of accepted crossovers. We stop at 25.

The radial adjustment is shown in Figure 4b. A four-parameter-per-orbit model (solid curve) follows the once-per-rev variations closely but cannot track rapid transitions as well as 8-parameter (dashed) or 16-parameter (dotted) models. The number of parameters required for significant improvement is discussed in section 4.

3.3. Estimation of Along- and Across-Track Errors

In profile mapping, a track intersection provides only one crossover residual, which does not determine a direction to shift a given track. Additional information comes from the slope and heading of the profile, from which the best displacement may still be estimated in an overdetermined sense. In the along-track direction a displacement of the profile will change the crossover by an amount proportional to the along-track slope, and in any direction, proportional to the projection of the local gradient vector. We use a right-handed Cartesian coordinate system given by the along-track direction, the across-track direction, and the vertical. The gradient is poorly resolved where tracks are nearly parallel. We therefore estimate it from the pair of slopes and azimuths using damped least squares [Menke, 1989]. From the local gradient, we obtain the partials of the vertical crossover error with respect to displacements. We parametrize these adjustments using the same basis as the radial errors, and scale them so that one standard deviation is equal to 10 ms of travel along-track, or 30 m. It is then straightforward to solve simultaneously for three parameter vectors using (8).

4. Results

Figure 5 shows histograms of the crossover error before and after adjustment, from analysis of 24 million crossovers, using eight parameters per revolution for each dimension (cf. Figure 4b). Of the initial set of crossovers, only 1.6% could not be fit within 10 m, and were rejected. Of the remaining crossovers the initial residuals are long-tailed (Figure 5a), only the central portion being shown. More than 15% exceed 10 m, and more than 4% exceed 20 m. The final residuals are highly compact. The root-mean-square (RMS) error is reduced nearly fivefold, while the median absolute error, scaled to one standard deviation for a normal distribution, is reduced nearly threefold, from 2.7 to 0.96 m. These numbers mainly reflect reduction in error in the central portion of the histogram, but we note that the initial errors were as large as 300 m before adjustment.

Table 2 shows RMS crossover residuals before and after adjustment for models with varying parameterizations and constraints. The number of acceptable crossovers and initial residuals differ slightly between models. A radial adjustment with 44,934 parameters (model a) results in the fewest acceptable crossovers and highest residual. Adjustment of the radial and along-track dimensions (model b) resulted in significantly lower residuals. The significance of fit of model b with m_b parameters relative to model a may be tested by $F_{ab} = [\chi_b^2 / (n_b - m_b - 1)] / [\chi_a^2 / (n_a - m_a - 1)]$. With over 24 million of observations, an F statistic greater than 1.001 is unlikely to result by chance at a 99% confidence level. Ad-

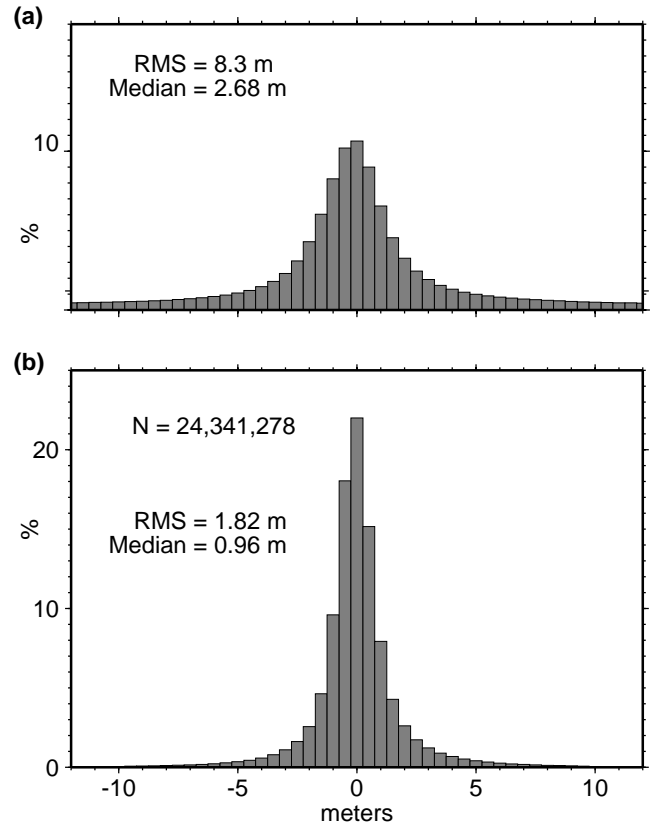


Figure 5. (a) Initial and (b) final histograms of altimetric residual for crossovers accepted by preferred model d.

dition of across-track adjustment (models c-i) significantly improves residuals. Model c uses fewer total parameters but provides a better fit than model b. Our preferred solution, in terms of data fit and stability near data gaps, is given by model d, an adjustment of ground tracks in three dimensions.

Using eight parameters per revolution, i.e., fitting once- and twice-per-rev errors and offsets, results in significantly lower residuals than with only four parameters per revolution (model c). The number of observations n_d exceeds the number of parameters by a factor of 200. These parameters are overdetermined by the data, in that a tighter a priori orbit sigma (model e) produces virtually the same residual. Additional parameters, as in models f-i, produce more complex models (cf. Figure 4b, dotted curve), with less dramatic improvements. Models f-i show additional ability to resolve transient changes, such as momentum dumps and pointing anomalies.

The formal model parameter covariance, for crossover

Table 2. Crossover residuals and significance of parametrization^a

Model	Initial	Adjusted	F	m	n	% accepted	Notes
a	7.836	2.510	—	44,934	23,792,751	96.2	8 parameters/revolution, radial only
b	8.211	1.995	1.580	89,868	24,259,210	98.1	8 parameters/rev., radial/along-track
c	8.247	1.899	1.105	67,404	24,299,702	98.3	4 parameters/rev., 3-D
d	8.303	1.817	1.089	134,802	24,341,278	98.4	8 parameters/rev., 3-D
e	8.303	1.818	1.001	134,802	24,341,104	98.4	8 parameters/rev., $\sigma_p=0.5$ m
f	8.303	1.808	1.007	202,212	24,350,659	98.5	12 parameters/rev., 3-D
g	8.319	1.791	1.024	269,598	24,365,049	98.6	16 parameters/rev., 3-D
h	8.360	1.752	1.033	539,184	24,402,468	98.7	32 parameters/rev., 3-D
i	8.437	1.704	1.033	1,078,368	24,446,666	98.8	64 parameters/rev., 3-D

^aResiduals in meters.

variance scaled to unity, is given by

$$C_{pp}^{final} = (G^T G + C_{pp}^{-1})^{-1}. \quad (9)$$

Given the formal (and observed) errors in each crossover on the order of one meter, the solutions generally have <20-cm uncertainty according to (9). Because the distributions of the orbital and data errors are complex and dominated by systematic errors, the formal measures might be misleadingly small.

Figure 6 shows the 3-D models for data on September 5, 1999. This day has particularly large-amplitude radial adjustments (solid lines). Following the first AMD (triangular symbol) the crossover error cycles with 10-m amplitude for six revolutions. Following two closely spaced AMDs, the amplitude increases to 15 m. After the final AMD the amplitude returns to nearly 0 and remains there until September 8 (cf. Figure 4).

Table 2 shows that adjustments in all three directions are required to fit the crossover data. The radial adjustments mainly consist of quasi-cyclic, once-per-rev perturbations. As shown in Figure 6, the phase, amplitude and offset of these adjustments change abruptly. The examples shown here correspond to large gaps in tracking. When tracking coverage is continuous, GEODYN fits AMD accelerations well and the radial adjustments are negligible, as in the early portion of Figure 4. The along-track adjustment (dashes) is less easily described. In general, these reflect a combination of pointing and timing errors as well as orbital errors, as discussed in the next section.

An important test of resolution is to recover a known displacement. Using altimetry the previous day, when tracking was good, we displaced four tracks on alternate orbits by 300 m both along and across track. Each 300 m could rep-

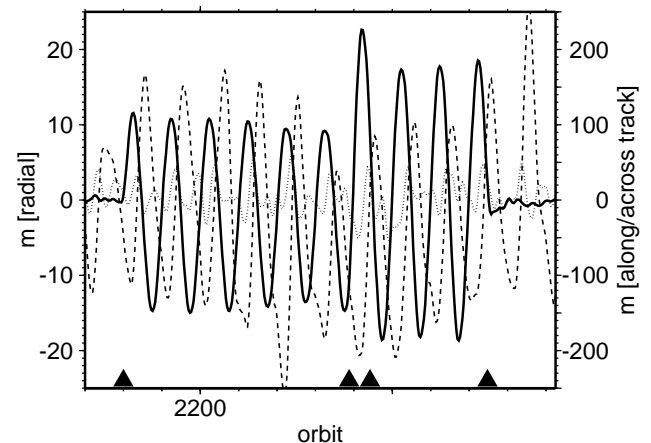


Figure 6. Preferred model for radial (solid), along-track (dashes), and across-track (dots) adjustments over a period of 1 day. Symbols show times of propulsive events.

resent an orbital error, a timing offset of one shot (0.1 s), a pointing bias of $750 \mu\text{rad}$, or an attitude timing bias of 1 s. Figure 7 shows the difference in crossover adjustment relative to non-perturbed tracks. Recovery of the along-track perturbation is best at the poles, where crossovers are densest. Less than half of the prescribed across-track displacement is recovered. Poor recovery is chiefly due to the large displacement and the small angle of crossing of ground tracks.

Such large, discontinuous changes in position are atypical. They exceed the range of validity of the linearized adjustment scheme, and introduce correlations with radial

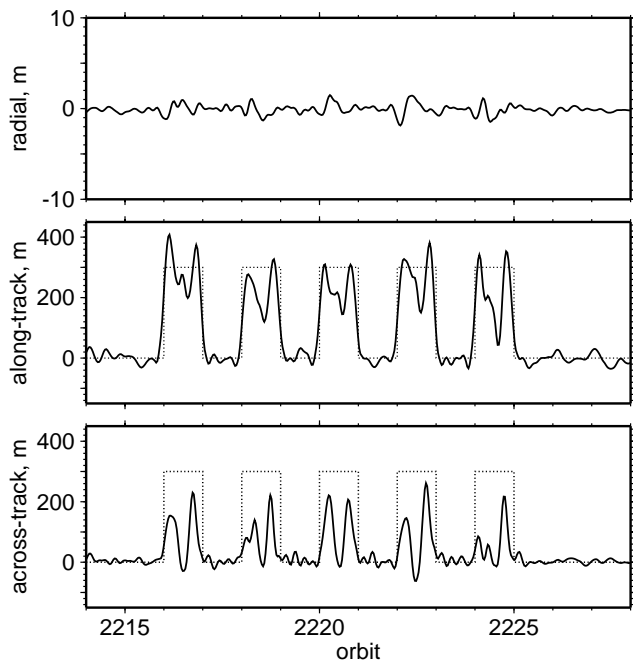


Figure 7. Model adjustment solution from four tracks that have been displaced on alternate orbits by 300 m along two components.

errors. The radial adjustment changes from the nominal solution by as much as a meter. Iterating the crossover analysis with relocated tracks might eventually converge, but this was not attempted. Most importantly, the misregistration of the ground tracks is flagged as relatively large and provides a basis for further investigation. In the data considered here, positional corrections are typically 100 m along-track and 20 m across-track. Large excursions occur much less than 1% of the time and are edited from global grids.

4.1. Short-Term Errors

In our 3-D example on this day, the periodic along-track adjustment (Figure 6, dashes) is nearly 150 m in amplitude. Although a twice-per-revolution parametrization adequately models radial errors, the along-track adjustment is best resolved by incorporating more parameters. Figure 8, dashes, shows the average periodic component of the along-track solution as a function of orbital argument, using 64 parameters per revolution. On the descending pass, starting from the equator at 0°, pitch deviates very little until ~75°S. The true laser position moves nearly half a shot behind the nominal position as it approaches the south pole. On the ascending pass, the position moves half a shot ahead, then recovers. A variation of nearly 200 m occurs over the

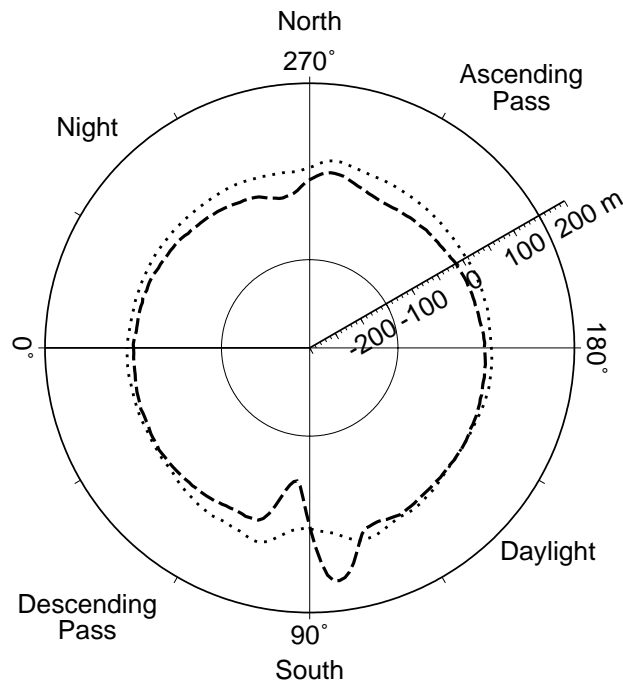


Figure 8. Polar plot of the along-track (dashes) and across-track (dots) position error as a function of orbital argument, averaged over three months (September-November 1999). Descending node is 0°, ascending node is 180°.

south pole, and a smaller variation over the north pole. The amplitude and phase of these variations are similar on each revolution, amounting to an error of nearly one shot spacing. The short duration of this anomaly can only be resolved within the time span of one parameter, ~7 min. The across-track adjustment (Figure 6, dots) is smaller in amplitude, and positively correlated with the along-track adjustment. Some of the variation is random, but averaged over many orbits, pointing knowledge is clearly perturbed during passage over the poles. The laser heat sink records significant temperature excursions with respect to orbital environment. The greater magnitude of the pointing variation when crossing from night to day is consistent with a thermal origin.

4.2. Long-Term Errors

Figure 9 shows the three components of the solutions smoothed over the duration of one day. Both radial and along-track components are erratic toward the end of the first mapping period. Tracking quality worsened as MGS approached solar conjunction (July 7, 2000) due to increased noise in the X-band Doppler, which resulted in larger orbit errors. Events such as targeting campaigns for the Mars Po-

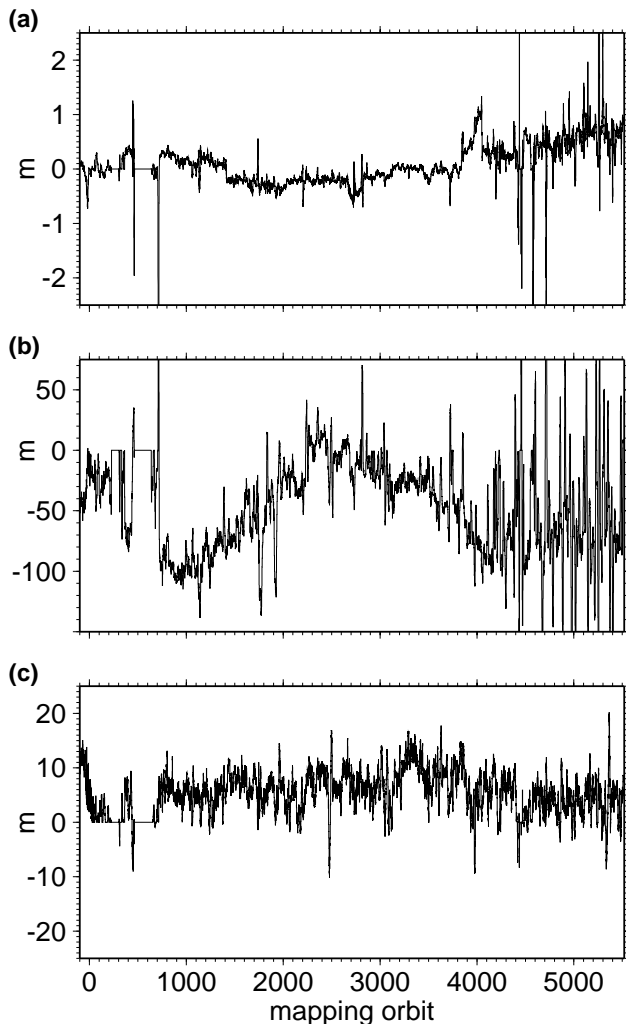


Figure 9. (a) Radial component of crossover model, median-averaged over 24-hour windows, as a function of mapping orbit. (b) Along-track model, averaged. (c) Across-track model, averaged.

lar Lander during mapping orbits circa 3400-4100 also cause temporary degradation in quality. During these campaigns, the attitude control system was commanded to a different mode and nadir-pointing operation was interrupted repeatedly. Because pointing errors affect off-nadir observations dramatically, altimetric quality suffered.

There are minuscule fluctuations in the radial average, reflecting overall ranging stability and orbit consistency. Spikes are generally end-effects where nadir coverage is interrupted for high-gain antenna tracking passes and targeting activities. The long-term radial measurement consistently lies within a 1-m envelope. Residual effects at the

sub-meter level would reflect variability in laser output and atmospheric conditions indirectly affecting the range measurements, or systematic errors in the semi-major axis of the MGS orbit.

The along-track anomaly (Figure 9b), after filtering out the cyclic variations discussed previously, averages -50 m. This represents a residual MOLA boresight alignment bias in the pitch direction and/or attitude timing bias. Along-track error varies over the 15-month duration of observations with ~ 50 -m amplitude, correlated with seasonal temperatures on MGS that peaked in November 1999. This pattern points to thermomechanical changes in alignment of the laser with respect to the MGS inertial reference frame, although small changes in laser beam pattern with temperature were also observed during pre-flight testing (R. Afzal, personal communication, 2000).

The across-track anomaly (Figure 9c) is positive, ~ 10 m on average, probably also a residual boresight bias. The position anomaly shows some systematic excursions, not seasonally controlled. The anomaly is underestimated (cf. Figure 7), but over a year, the across-track position was probably stable within 30 m.

4.3. Gridded Data Sets as a Means of Assessment

Gridded, relief-shaded data sets are used to verify the corrections and to identify questionable tracks. The adjustment values encoded in the MOLA PEDR standard data product are examined, and portions of tracks where on rare occasions the correction exceeds 450 m along-track, or 150 m across-track, are excluded. Radial adjustments greater than 40 m are also deemed unreliable.

In the polar regions, more than 50% of grid cells contain one or more MOLA shots at resolutions of 300 m (~ 1 shot spacing). Examples of north and south polar maps are shown in Figures 10 and 11. The digital terrain models have been artificially “shaded” using a directional derivative [Wessel and Smith, 1998], normalized by a cumulative Laplace distribution. This transformation accentuates small-scale features and subtle slope variations, as well as slight anomalies in tracks. Individual tracks are occasionally discernible due to interpolation. Occasional linear features reveal meter-level misfits of parallel tracks.

Such images provide an X-ray-like picture of the planet. Buried impact basins, ridges, troughs, and layering are revealed by their subtle slopes [Withers and Neumann, 2001]. The accuracy of slopes, measured over a baseline of one shot spacing, is ~ 1 in 10^3 , and is proportionately better over longer baselines.

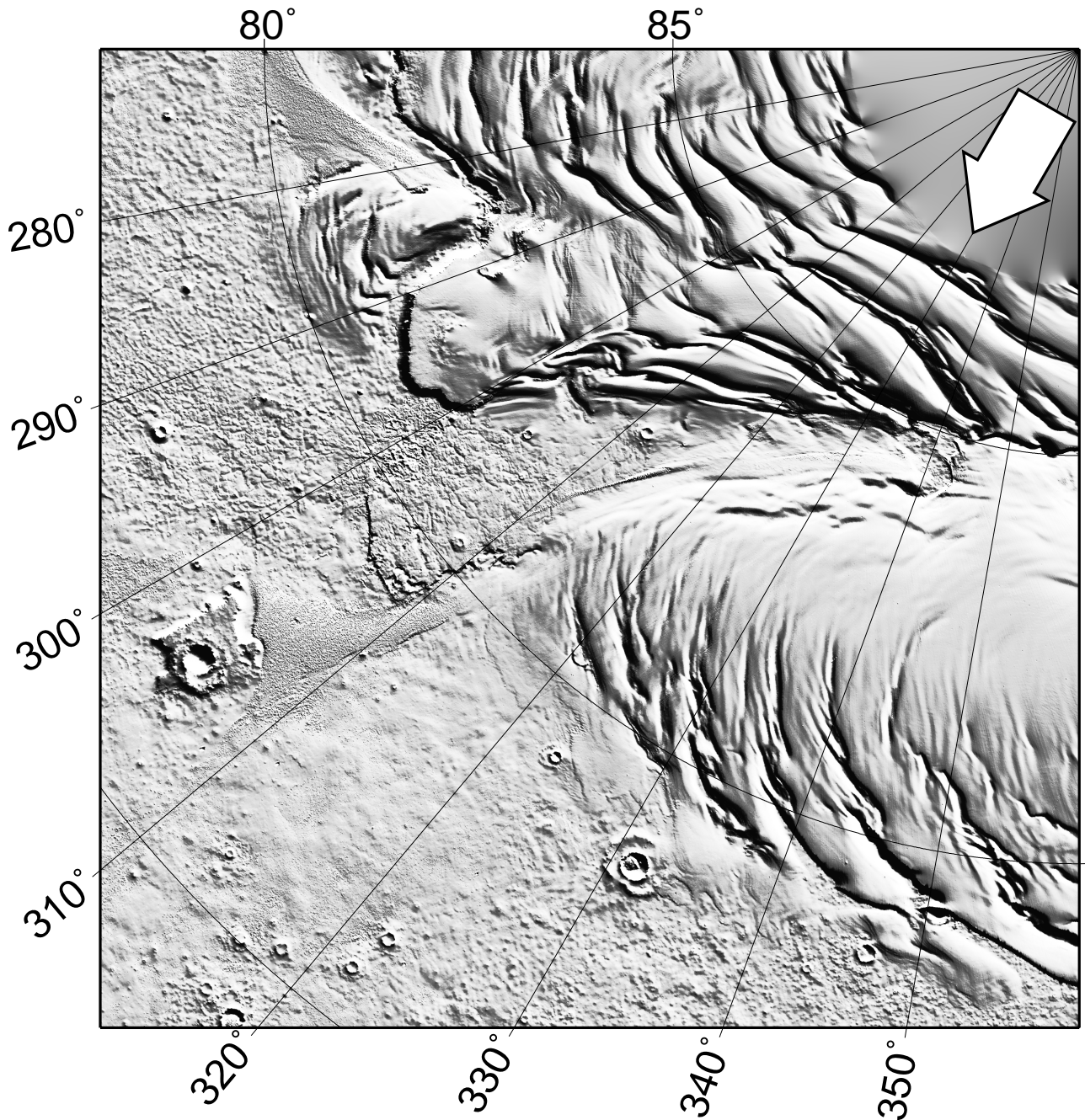


Figure 10. North polar cap. Gradient shading is from the direction indicated by the arrow. The image shows Chasma Boreale, and the surrounding polar layered terrain and plains. Undulations of a few meters are visible across the polar ice. Small volcanoes, usually poorly imaged due to polar haze, are visible in the upper-left corner. Craters on residual cap are only seen in topography. Polar stereographic projection subtends 12° of latitude, ~ 720 km square

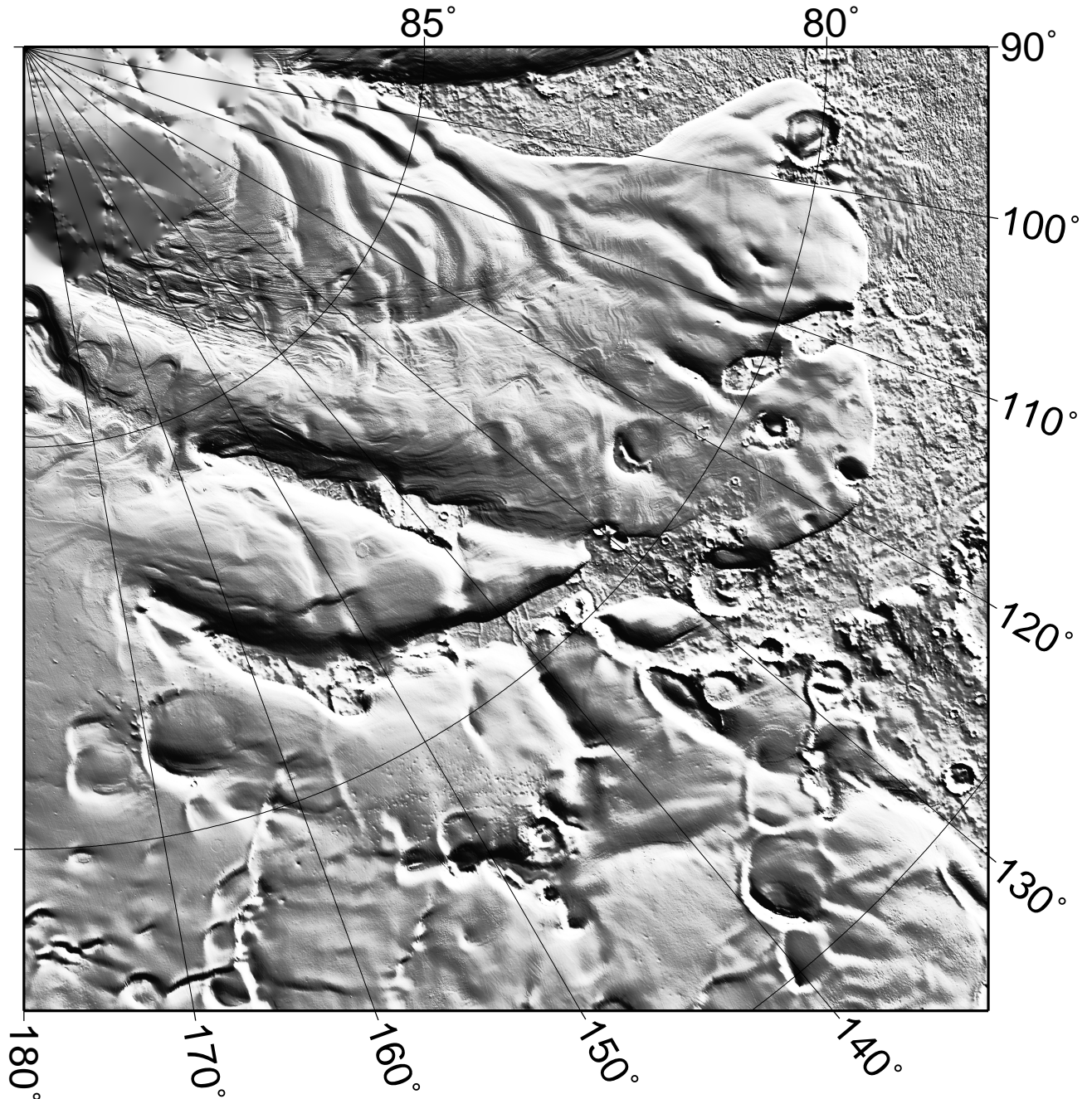


Figure 11. South polar cap. Shading, projection and scale as in 10. Chasma Australe at the top contains sinuous positive-relief features and partially covered rays surrounding a large crater. Many of the smallest depressions on the polar layered terrain are likely degraded craters. Complex layering of the residual cap is crosscut by remarkable, kilometer-scale striations running from left to right. Bottom of figure lies just poleward of Mars 1998 Polar Landing Site.

5. Discussion

Crossover misfit may result from planetary dynamics, as well as instrumental considerations. Solid body tides are

negligible at the distance of Mars from the Sun, but the seasonal deposition and sublimation of solid CO_2 may cause meter-level changes in the height of polar caps with season

[Smith *et al.*, 1999b]. The methods described here may be used to analyze such changes, while correcting for orbital errors, by restricting crossovers to latitudes lower than the polar frost line (D.E. Smith *et al.*, manuscript in preparation, 2001). Polar crossovers may be used to constrain shorter-period errors, provided their tracks occur within the same seasonal period, so that they measure similar amounts of deposition.

A challenge to measuring long-term changes in topography is the uncertainty in range correction. Systematic errors at the submeter level could result from differing amounts of saturated pulses and/or different proportions of pulses received on channels 1 and 2. Such errors should be most apparent during major dust storms, when atmospheric opacity causes dramatic changes in signal strength. A dusty atmosphere takes MOLA out of saturation and causes a later trigger in the time-of-flight measurement, thus appearing as slightly lower topography (cf. Table 1). Forward scattering by clouds (G.A. Neumann *et al.*, One Mars year of clouds detected by the Mars Orbiter Laser Altimeter, submitted to *Journal of Geophysical Research*, 2001) could also cause a later trigger in the time-of-flight measurement. Atmospheric opacity varies seasonally [Martin, 1986; Colburn *et al.*, 1989; Kahn *et al.*, 1992] so if not appropriately accounted for in the range walk correction, it could conceivably be mistaken for a temporal elevation change. Recent analysis to track seasonal variations in polar topography that incorporates information on the temporal state of the atmosphere (D.E. Smith *et al.*, manuscript in preparation, 2001) indicates that such corrections can be effectively applied.

Cumulative errors in the orientation of Mars, i.e., variation in the planet's length of day arising from volatile exchange and global circulation of the atmosphere, may also cause misfit. A periodic variation with season of 1 ms in length of day would produce variations in the longitudinal position of the prime meridian with respect to the IAU1991 model of 25 m over the course of a year. This would cause a once-per-revolution error in the across-track position. Length of day variations on Mars have been measured from analysis of the Martian gravity field with resolution of 1 ms or less (D.E. Smith *et al.*, manuscript in preparation, 2001). The use of the crossover anomalies to measure variations in length of day has so far been difficult, but given their sensitivity to small changes in the rotational rate, changes in position of profiles with respect to the prime meridian may eventually be tracked.

The quality of the reconstructed spacecraft state and attitude, combined with the precision of the MOLA ranges, provides accuracy in planetary measurement beyond mission specifications. We have refined the attitude during nadir operation, and can discern a residual bias of ~ 10 m (25 mrad)

across-track and ~ 50 m (125 mrad) along-track. These biases are small compared to the size of the laser footprint, and are correctable to a great extent. In general, the corrections become poor when they exceed the spacing of shots. These few portions of the data are removed when selecting profiles for map display. Some of these portions may be recovered through iterative refinement. Since corrections larger than 100 m seldom occur, overall accuracy is bounded by this amount.

The accuracy of MGS timing remains a concern for studies of planetary dynamics. A 12-ms error in the clock conversions, or 0.12 s in attitude timing bias, can result in 36 m of constant along-track misfit, and 0.8 m of cyclic error radially. These errors have been removed implicitly by the adjustment of tracks at crossovers with a twice-per-revolution correction [e.g., Shum *et al.*, 1990].

6. Conclusions

The largest single contribution to orbital error currently results from spacecraft propulsive maneuvers. The lack of vector acceleration information from the MGS spacecraft mandates that these maneuvers be estimated dynamically. Gaps in tracking preclude this in many instances. Incorporation of altimetric crossovers into the orbit determination process can overcome this but is logistically time consuming. We have shown how these errors can be corrected after the fact in a relatively simple fashion.

The ranging accuracy of MOLA is maintained via timing analysis at centimeter level. Systematic errors in range walk correction are unavoidable, due to the limited dynamic range of instrumental parameters, but the scale of such errors is comparable to the measurement precision and orbital accuracy. Range correction errors must be considered when examining seasonal variations in topography.

The ability to measure positions on Mars with the precision obtained in this study is unprecedented. Previous knowledge of the positions of images taken during the Viking missions suffered from errors in excess of 15 km [Smith *et al.*, 1999a], and even for the well-studied Pathfinder site, the location of the landing site with respect to images as determined by different groups [Duxbury, 1995; Zeitler and Oberst, 1999] shows a difference of 5 km. After accounting for systematic errors we reduce crossover errors to insignificant levels with overwhelming numbers of data points that are individually placed with respect to Mars' center of mass. A preliminary covariance analysis, as well as the systematics shown in Figure 9, indicate random errors in position, after correction, well under 100 m, and certainly smaller than the ~ 168 -m laser footprint.

The RMS residual crossover error of 1.8 m is a very con-

servative estimate of the actual uncertainty, since even if orbits, ranges, and pointing were perfectly known, a certain level of error would be expected due to undersampling of the Martian terrain. Moreover, the bulk of the crossovers are fit to within 0.96 m (Figure 5). The actual quality of the ground tracks must be better than the RMS crossover residual. Since each crossover represents a difference of two independent measurements, the uncertainty in any individual measurement is therefore 1.3 m. Point-to-point variation in topography is seldom less than 1 m, so undersampling is probably responsible for at least as much error as orbital and measurement uncertainty. This being the case, individual measurement consistency at the same location is typically better than 1 m. The accuracy of each measurement is probably about the same, since systematic errors in range measurement have been bounded by inter-channel comparisons to at most 1 m. Any systematic error in the orbit of MGS is probably on the order of the precision of the gravitational potential GM and low-degree harmonic terms, which are known to better than 10^{-7} , or ~ 0.4 m at the radius of MGS. A full determination of the systematic error may await the placement of retro-reflector landmarks on Mars, but where a MOLA profile has passed within 100 m of a lander (Viking 2) of well-determined elevation [Folkner *et al.*, 1997], the discrepancy in elevation was essentially zero [Smith *et al.*, 1999c].

Appendix A: Timing

We use the MOLA data stream to compare MOLA's time source to that of the spacecraft, and provide an absolute range calibration. Laser firing and time-of-flight measurements are derived from the MOLA master clock, a stable, temperature-controlled oscillator whose frequency f_m is nominally 100 MHz. MOLA prepares data packets each 140 shots, commanded by a 10-Hz interrupt generated by the clock. The Payload Data System (PDS) queries packets every 14 s. The actual frequency, measured preflight at 99,996,280 Hz, was chosen so that the time between instrument packets would be slightly longer than 14 s, so that occasional dummy packets would be sent but no data would be lost. This difference allows us to estimate the oscillator frequency relative to the PDS clock within one part in 10^8 . The PDS time is converted to ephemeris time seconds from J2000 (ET) via Project-supplied clock kernels [Thorpe *et al.*, 1995], essentially linear interpolants from bimonthly waypoints. These conversions may drift from actual time by 12 ms or more.

Each science packet has a sequential identifier i cycling from 0 to $2^{14} - 1$, and records two time signals: a packet time code P received from the PDS, with a resolution of one second, and a fine time code M , with a resolution of $1/256$ s (one "tick"), generated by a counter on board MOLA driven by an oscillator synchronized to the PDS 8-Hz interrupts.

The start time t_i of the i th packet is

$$t_i = P + M/256 + \epsilon, \quad (\text{A1})$$

where ϵ is a nonnegative delay between the last tick and the packet start. In the eccentric orbits of the science phasing period, where the radial distance to Mars varies by up to 1600 m s^{-1} , precision better than $1/256$ s is desired. The time t of the j th shot is a linear function:

$$t = t_i + \frac{10^7}{f_m}(j - 1). \quad (\text{A2})$$

As discussed in the introduction, in all subsequent MOLA processing, it is assumed that the actual laser fire time is 117 ms after the time recorded in the Precision Experiment Data Record (PEDR).

It is convenient to express t_i in terms of a reduced time (drift) from the nominal time 14i:

$$t_i = a + bi + 14i, \quad (\text{A3})$$

where a , b , are constants to be determined on a daily basis. The constant b is the drift per packet with respect to a nominal packet time interval of 14 s, related to the clock frequency by

$$f_m = \frac{14 \times 10^8}{b + 14} \quad (\text{A4})$$

If the error ϵ were entirely due to quantization, it would be uniformly distributed in the range $[0 - 1/256]$. Estimation of true time can be posed as a linear feasibility problem:

Find a , b , d such that

$$a + bx_i \geq t_i - 14i \quad (\text{A5a})$$

$$a + bx_i - d \leq t_i - 14i \quad (\text{A5b})$$

$$a, b, d \geq 0. \quad (\text{A5c})$$

If ϵ were randomly distributed, a maximum likelihood estimate [Tarantola, 1987] of a and b would minimize d . When the linear relationship in (A3) is exact, $d < 1/256$. The standard linear programming problem, where the objective function, $-d$, is maximized subject to the above constraints, is solved via the Simplex Algorithm [Dantzig, 1963] as implemented by Press *et al.* [1992]. The time signals, especially M , are subject to occasional, hardware-related bit errors. These result in values of d much greater than one tick and must be corrected before analysis.

Figure A1a shows the reduced MOLA packet time in ticks vs. time for each packet in pass 3, the first data over

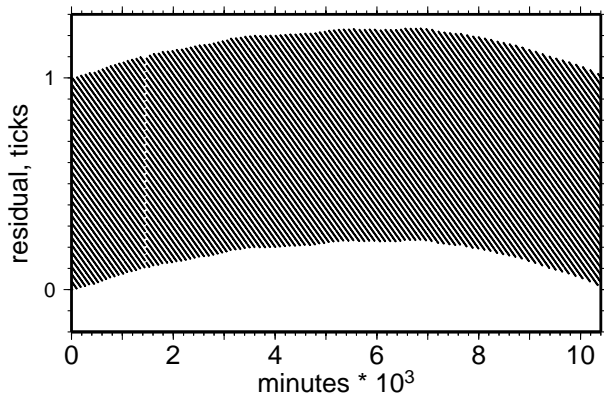


Figure A2. MOLA oscillator drift over a 7-day period in mapping, May 2000.

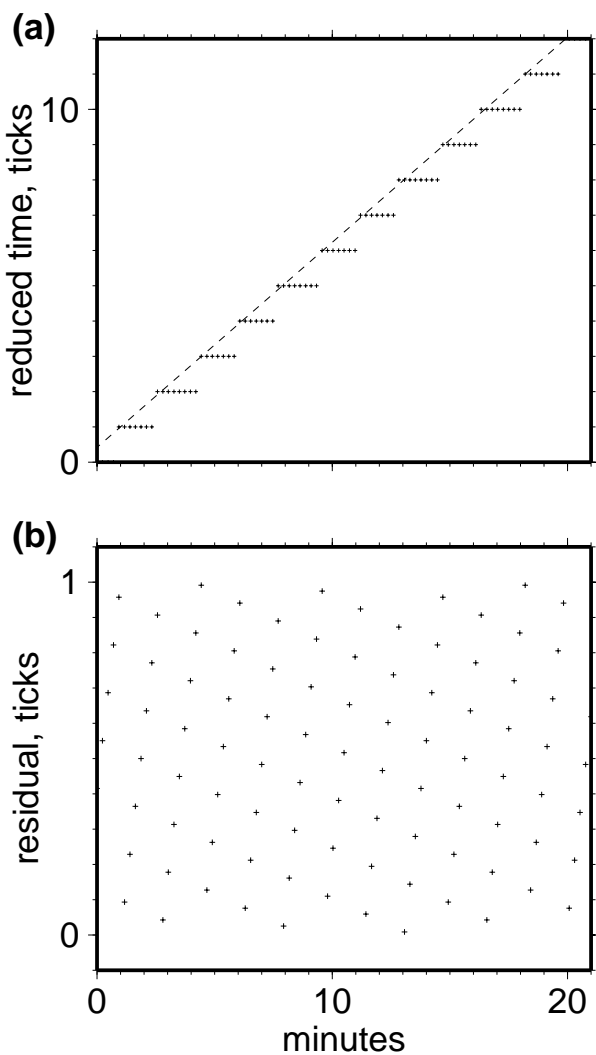


Figure A1. (a) Reduced time of packets. (b) Residual after linear fit to times in Figure A1a.

Mars. The shot times ideally lie along the dashed line, with slope b , within a few microseconds. Figure A1b shows the residual time errors ϵ . Over the course of a mapping day the residual envelope may curve slightly due to temperature fluctuations.

Figure A2 shows the behavior of the MOLA oscillator relative to the spacecraft clock over a period of 7 days. A gradual decrease in frequency with time causes the residual to curve downward. Stability over this period was ~ 0.8 ms (0.2 ticks). Evidently the daily variation is much less than 1 part in 10^8 . The precise frequency is estimated daily [Smith *et al.*, this issue, Figure 2] and used to convert MOLA range counts to time.

Acknowledgments. The MOLA investigation is supported by the NASA Mars Exploration Program. Reviews by W.H.F. Smith and P. Wessel, as well as informal reviews by T. Duxbury and X. Sun, greatly improved the paper. We recognize significant contributions from J. B. Abshire, R. Afzal, J. B. Blair, and J. Zwally. The Generic Mapping Tools software [Wessel and Smith, 1998] facilitated the analysis.

References

Abshire, J. B., X. Sun, and R. S. Afzal, Mars Orbiter Laser Altimeter: Receiver model and performance analysis, *Appl. Opt.*, 39, 2440–2460, 2000.

Acton, C. H., Jr., Ancillary data services of NASA’s navigation and ancillary information facility, *Planet. Space Sci.*, 44, 65–70, 1996.

Afzal, R. S., Mars Observer Laser Altimeter: Laser transmitter, *Appl. Opt.*, 33, 3184–3188, 1994.

Albee, A. A., R. E. Arvidson, and F. D. Palluconi, Mars Observer mission, *J. Geophys. Res.*, 97, 7665–7680, 1992.

Colburn, D., J. Pollock, and R. Haberle, Diurnal variations in the optical depth at Mars, *Icarus*, 79, 159–189, 1989.

Dantzig, G. B., *Linear Programming and Extensions*, Princeton Univ. Press, Princeton, N.J., 1963.

Davies, M. E., V. K. Abalakin, A. Brahic, M. Bursa, B. H. Chovitz, J. H. Lieske, P. K. Seidelmann, A. T. Sinclair, and Y. S. Tjuflin, Report of the IAU/IAG/COSPAR working group on cartographic coordinates and rotational elements of the planets and satellites: 1991, *Cel. Mech. Dyn. Astron.*, 53, 377–397, 1992.

Duxbury, T. C., Preliminary cartographic analysis of the Pathfinder landing site using Viking Orbiter images, in *Mars Pathfinder Landing Site Workshop II: Characteristics of the Ares Vallis Region and Field Trips in the Channeled Scabland*, Washington, edited by M. P. Golombek, K. S. Edgett, and J. W. Rice, Jr., *LPI Tech. Rep. 95-01*, Part 2, pp. 35–36, Lunar and Planet. Inst., Houston, 1995.

- Folkner, W. M., C. F. Yoder, D. N. Yuan, E. M. Standish, and R. A. Preston, Interior structure and seasonal mass redistribution of Mars from radio tracking of Mars Pathfinder, *Science*, 178, 1749–1751, 1997.
- Gardner, C. S., Ranging performance of satellite laser altimeters, *IEEE Trans. Geosci. Remote Sens.*, 30, 1061–1072, 1992.
- Garvin, J. B., J. L. Bufton, J. B. Blair, D. Harding, S. B. Luthcke, J. J. Frawley, and D. D. Rowlands, Observations of the Earth's topography from the Shuttle Laser Altimeter (SLA): Laser pulse echo recovery measurements of terrestrial surfaces, *Phys. Chem. Earth*, 23, 1053–1068, 1998.
- Kahn, R. A., T. Z. Martin, R. W. Zurek, and S. W. Lee, The Martian dust cycle, in *Mars*, edited by H. H. Kieffer, B. M. Jakosky, C. W. Snyder, and M. S. Matthews, pp. 1017–1053, Univ. of Ariz. Press, Tucson, 1992.
- Lemoine, F. G., The dynamics of orbiting satellites and gravity model development, Ph.D. thesis, Univ. of Colo., Boulder, 1992.
- Lemoine, F. G., D. D. Rowlands, D. E. Smith, D. S. Chinn, D. E. Pavlis, S. B. Luthcke, G. A. Neumann, and M. T. Zuber, Orbit determination for Mars Global Surveyor during mapping, *AIAA*, pp. 99–328, 1999.
- Lemoine, F. G., D. E. Smith, D. D. Rowlands, M. T. Zuber, G. A. Neumann, D. S. Chinn, and D. E. Pavlis, An improved solution of the gravity field of Mars (GMM-2B) from Mars Global Surveyor, *J. Geophys. Res.*, this issue.
- Luthcke, S. B., D. D. Rowlands, J. J. McCarthy, E. Stoneking, and D. E. Pavlis, Spaceborne laser-altimeter-pointing bias calibration from range residual analysis, *J. Spacecr. Rockets*, 37, 374–384, 2000.
- Marshall, J. A., N. P. Zelensky, S. M. Klosko, D. S. Chinn, S. B. Luthcke, K. E. Rachlin, and R. G. Williamson, The temporal and spatial characteristics of TOPEX/POSEIDON radial orbit error, *J. Geophys. Res.*, 100, 25,331–25,352, 1995.
- Martin, T. Z., Thermal infrared opacity of the Martian atmosphere, *Icarus*, 66, 2–21, 1986.
- McGarry, J. F., L. K. Pacini, J. B. Abshire, and J. B. Blair, Design and performance of an autonomous tracking for the Mars Observer Laser Altimeter, *Conf. Lasers Electro-Optics*, 10, CThR27, 1991.
- Menke, W., *Geophysical Data Analysis: Discrete Inverse Theory*, Academic, San Diego, Calif., 1989.
- Nishimura, C. E., and D. W. Forsyth, Improvements in navigation using Sea Beam crossing errors, *Mar. Geophys. Res.*, 9, 333–352, 1988.
- Pavlis, D. E., S. Luo, P. Dahirop, J. J. McCarthy, and S. B. Luthcke, GEODYN operations manuals, Raytheon ITSS Contractor Report, Greenbelt, Md., March 26, 1999.
- Press, W. J., B. P. Flannery, S. A. Teukolsky, and W. T. Vetterling, *Numerical Recipes in FORTRAN: The Art of Scientific Computation*, Cambridge Univ. Press, New York, 1992.
- Prince, R. A., and D. W. Forsyth, A simple objective method for minimizing crossover errors in marine gravity data, *Geophysics*, 49, 1070–1083, 1984.
- Rowlands, D. D., D. E. Pavlis, F. G. Lemoine, G. A. Neumann, and S. B. Luthcke, The use of crossover constraint equations derived from laser altimetry in the orbit determination of Mars Global Surveyor, *Geophys. Res. Lett.*, 26, 1191–1194, 1999.
- Shum, C. K., B. H. Zhang, B. E. Schutz, and B. D. Tapley, Altimeter crossover methods for precision orbit determination and the mapping of geophysical parameters, *J. Astronaut. Sci.*, 38, 355–368, 1990.
- Smith, D. E., M. T. Zuber, G. A. Neumann, and F. G. Lemoine, Topography of the Moon from the Clementine lidar, *J. Geophys. Res.*, 102, 1591–1611, 1997.
- Smith, D. E., et al., Topography of the northern hemisphere of Mars from the Mars Orbiter Laser Altimeter (MOLA), *Science*, 279, 1686–1692, 1998.
- Smith, D. E., W. L. Sjogren, G. L. Tyler, G. Balmino, F. G. Lemoine, and A. S. Konopliv, The gravity field of Mars: Results from Mars Global Surveyor, *Science*, 286, 94–96, 1999a.
- Smith, D. E., M. T. Zuber, R. M. Haberle, D. D. Rowlands, and J. R. Murphy, The Mars seasonal CO₂ cycle and the time variation of the gravity field: A General Circulation Model simulation, *J. Geophys. Res.*, 104, 1885–1896, 1999b.
- Smith, D. E., et al., The global topography of Mars and implications for surface evolution, *Science*, 284, 1495–1503, 1999c.
- Smith, D. E., et al., Mars Orbiter Laser Altimeter: Experiment summary after the first year of global mapping of Mars, *J. Geophys. Res.*, this issue.
- Tarantola, A., *Inverse Problem Theory*, Elsevier, New York, 1987.
- Tarantola, A., and B. Valette, Generalized nonlinear inverse problems solved using the least squares criterion, *Rev. Geophys.*, 20, 219–232, 1982.
- Thorpe, T. E., A. Albee, G. D. Pace, S. S. Dallas, and G. E. Cunningham, *Mars Global Surveyor Investigation Description and Science Requirements Document*, vol. JPL D-12487, Jet Propul. Lab., Pasadena, Calif., 1995.
- Ullman, R., SOLVE program mathematical formulation, *Tech. Rep. HSTX/GG-9201*, Raytheon ITSS, Greenbelt, Md., 1997.
- Wessel, P., XOVER: A cross-over error detector for track data, *Comput. Geosci.*, 15, 333–346, 1989.
- Wessel, P., and W. H. F. Smith, New, improved version of Generic Mapping Tools released, *Eos Trans. AGU*, 79, 579, 1998.
- Withers, P., and G. A. Neumann, Enigmatic northern plains of Mars, *Nature*, 410, 651, 2001.
- Zeitler, W., and J. Oberst, The Mars Pathfinder landing site and the Viking control point network, *J. Geophys. Res.*, 104, 8935–8941, 1999.
- Zuber, M. T., D. E. Smith, S. C. Solomon, D. O. Muhleman, J. W. Head, J. B. Garvin, J. B. Abshire, and J. L. Bufton, The Mars Observer Laser Altimeter investigation, *J. Geophys. Res.*, 97, 7781–7797, 1992.
- Zuber, M. T., D. E. Smith, F. G. Lemoine, M. H. Torrence, P. J. Dunn, J. B. Abshire, and J. L. Bufton, Rotational dynamics, time-varying gravity and the seasonal cycle of CO₂ on Mars, *Eos Trans. AGU*, 81 (19), Spring Meet. Suppl., S292, 2000.
- F. G. Lemoine, G. A. Neumann, D. D. Rowlands, and D. E. Smith, Laboratory for Terrestrial Physics, Code 920, NASA Goddard Space Flight Center, Greenbelt, MD 20771. (Gregory.Neumann@gssc.nasa.gov)
- M. T. Zuber, Department of Earth, Atmospheric and Planetary Sciences, Massachusetts Institute of Technology, Building 54, 77 Massachusetts Avenue, Cambridge, MA 02139-4307.